inorganics

MDPI

Article

Ni(II) Complexes of 2-Imine-8-Hydroxyquinolines: Characterization, Albumin Binding and Cytotoxicity

Sofia Marcão [1,†], Leonor Côrte-Real [1,†], Alice Alborghetti [1], Maël Dejoux [1], Gabriella Spengler [2], Xavier Fontrodona [3], Isabel Romero [3], Éva A. Enyedy [4], Alexandra M. M. Antunes [1] and Isabel Correia [1,*]

[1] Centro de Química Estrutural and Departamento de Engenharia Química, Institute of Molecular Sciences, Instituto Superior Técnico, Universidade de Lisboa, Av. Rovisco Pais 1, 1049-001 Lisboa, Portugal; sofiadvmarcao@tecnico.ulisboa.pt (S.M.); leonor.corte-real@tecnico.ulisboa.pt (L.C.-R.); alexandra.antunes@tecnico.ulisboa.pt (A.M.M.A.)

[2] Department of Medical Microbiology, Albert Szent-Györgyi Health Center and Albert Szent-Györgyi Medical School, University of Szeged, Semmelweis u. 6, H-6725 Szeged, Hungary; spengler.gabriella@med.u-szeged.hu

[3] Departament de Química i Serveis Tècnics de Recerca, Universitat de Girona, C/M Aurèlia Capmany, 69, E-17003 Girona, Spain; marisa.romero@udg.edu (I.R.)

[4] Department of Molecular and Analytical Chemistry, University of Szeged, Dóm tér 7-8., H-6720 Szeged, Hungary

* Correspondence: icorreia@tecnico.ulisboa.pt

† These authors contributed equally to this work.

Abstract

Nickel(II) offers an appealing base for metallodrug design as it is abundant, inexpensive and forms well-defined complexes with N,O-donor ligands. Therefore, five Ni(II) complexes containing two tridentate 2-imine-8-hydroxyquinoline Schiff base ligands, derived from morpholine, piperidine, imidazole or 2-methyl-1*H*-limidazole, were synthesized and characterized in solution and solid state via analytical and spectroscopic techniques. Single crystals were solved using X-ray diffraction for the complex derived from 4-(2-aminopropyl)morpholine (**1**). This Ni(II) complex exhibits a distorted octahedrally coordinated Ni(II) center bound to two monodeprotonated NNO-tridentate ligands, adopting a meridional coordination mode, with the two oxygen atoms arranged cis to each other. The stability of the complexes in aqueous media buffered at pH 7.4 was evaluated with UV–Vis spectroscopy and their binding to bovine serum albumin (BSA) was assessed with fluorescence titrations. All complexes show strong reversible binding to BSA (K_{SV} ~10^5), which stabilizes the lipophilic complexes in aqueous media. The antiproliferative activity of the complexes was screened against colon cancer cell lines (Colo205 and Colo320). They exhibit moderate anticancer activity (IC_{50} = 15.1–92.5 μM), with structure–activity relationships favoring imidazole derivatives and maintaining activity against the doxorubicin-resistant cell line (Colo320) with resistance indices (1.3–3.1) comparable to or lower than doxorubicin. Overall, the complexes represent a platform to develop new anticancer Ni-based drugs.

Keywords: Nickel(II); 8-hydroxyquinoline; Schiff bases; albumin binding; colon cancer

Academic Editors: Jun-Long Zhang, Yuncong Chen and Xuncheng Su

Received: 16 July 2026
Revised: 4 September 2026
Accepted: 5 September 2026
Published: 10 September 2026

1. Introduction

The clinical success of platinum chemotherapy has established metal complexes as viable anticancer agents. However, dose-limiting toxicities, acquired resistance and side effects continue to motivate the search for non-platinum metallodrugs with distinct intracellular targets and improved selectivity [1,2]. In this context, first-row transition metals

offer cost advantages and a rich coordination chemistry, enabling ligand-guided control of redox behavior, stability and biomolecular interactions [3–5].

Although nickel has historically received less attention in anticancer drug discovery due to its association with toxicity and carcinogenicity in some exposure contexts [6], numerous studies have shown that Ni(II) complexes exhibit antiproliferative properties [7,8] and engage in therapeutically relevant pathways, such as inhibiting the ubiquitin–proteasome system [9]. A Ni(II) complex containing 1,10-phenanthroline and different *N*,*N*-diethyldithiocarbamates was able to kill osteosarcoma and osteosarcoma stem cells via necroptosis (an ordered form of necrosis) at micromolar concentrations [10]. Similar findings were obtained for a nickel complex containing 3,4,7,8-tetramethyl-1,10-phenanthroline and two flufenamic acid moieties [11]. Another Ni(II) mixed ligand complex of 2,2′-bipyridine and febuxostat (a drug used to lower hyperuricemia) showed the strongest inhibitory effect in colon HTC 116 cancer cells, outperforming the reference doxorubicin as well as the corresponding Fe(III), Mn(II) and Co(II) complexes [12]. A distinct design logic is emerging in which the photophysics of square-planar Ni(II) is exploited directly: organonickel(II) macrocycles bearing strong σ-donating Ni–C bonds absorb in the near-infrared and function as phototheranostics, integrating photothermal therapy with photothermal and photoacoustic imaging in vivo [13], while a light-activated Ni(II)–ciprofloxacin conjugate uses localized hyperthermia at the metal center to potentiate antibiotic action and eradicate MRSA in a murine model [14]. Taken together, these findings suggest that ligand architecture—coordination geometry, metal–ligand covalency, and speciation control—is central to transforming nickel from a 'risk metal' into a therapeutic metal species.

8-Hydroxyquinoline (8HQ) is a privileged N,O-chelating scaffold with a long history of bioactivity and a demonstrated capacity to generate metal complexes with enhanced anticancer effects [15–18]. Our group has reported on a considerable number of metal complexes containing 8HQ derived molecules with promising antiproliferative effects towards different cancer cell lines [19–25]. Moreover, clinically used 8HQ derivatives such as clioquinol and nitroxoline further emphasize the translational relevance of this chemical space [26,27].

Many 8HQ nickel complexes showing relevant antiproliferative activity have been prepared. Mixed ligand complexes of Ni(II), Co(II), and Mn(II) containing 8HQ and 2-(((4-fluorophenyl)imino)methyl)-4-methoxy-6-nitrophenol were screened against A549 lung cancer cells and BEAS-2B normal bronchial epithelial cell lines [28]. The nickel complex exhibited high cytotoxic activity (IC_{50} = 5.97 μM), showing a lower IC_{50} than cisplatin and all other metal complexes in the studied series. Moreover, it showed no cytotoxicity towards the normal epithelial cells. A dinuclear Ni(II)-complex containing 5,7-Cl-8HQ was tested against liver (BEL7404), gastric (SGC7901) and breast (MCF-7) human cancer cell lines, demonstrating a considerable inhibition effect with IC_{50} values in the range 13.0–29.8 μM [29]. A study on 22 mixed ligand Ni(II)-complexes of different 8HQs and 1,2-bipyridine and 1,10-phenanthroline derivatives reported their antiproliferative activity after 24 h of incubation against A549 and A549/DDP tumor cells as well as normal HL-7702 cells, with most complexes showing cytotoxic activity in the low micromolar range. The complex derived from 2-Me-5,7-Cl-8HQ and 4,7-phenyl-1,10-phenanthroline was identified as the most promising one, inducing A549/DDP cell death mainly *via* mitophagy pathways [30]. Zhen-Feng Che and co-workers reported the cytotoxicity of Cu(II) and Ni(II) complexes of 2-((2-(pyridin-2-yl)hydrazono)methyl)quinolin-8-ol. Although the Cu(II) complex was more potent than the Ni(II) analogue in all cancer cell lines, the nickel complex displayed higher cytotoxicity than cisplatin in T24 bladder cancer cells [31].

Our group has been developing 8HQ-derived ligands incorporating an imine functionality at the 2-position, coordinating them with metal ions, including Ni(II), and assessing

their potential for anticancer therapy. A Schiff base (H_2L) obtained from the condensation of 2-CHO-8HQ with 2-hydrazinobenzothiazole was reacted with different transition metal ions, including nickel, for which [Ni(HL)(acetate)] and [$Ni(HL)_2$] were obtained [32]. Based on the promising cytotoxic activity, [Ni(HL)(acetate)] and a Ru(II) complex were further studied to evaluate their therapeutic window towards colon cancer and mechanisms of cell death. Both complexes were cytotoxic against human (HCT-116) and murine (CT-26) colon cancer cells (IC_{50} values < 21 μM) and exhibited superior potency when compared to the positive control, 5-fluorouracil (5-FU). Additionally, cell cycle was arrested in S phase in CT-26 cells upon incubation with the Ni-complex, which also inhibited cell migration in the HCT-116 cell line.

Recently we reported on Fe(III), V(IV) and Ni(II) complexes containing Schiff bases derived from 2-CHO-8HQ and 4-(2-aminoethyl)morpholine, among other amines. The metal complexes cytotoxicity was screened on melanoma (B16F10 and A375) and colon cancer (CT-26 and HCT-116), with 5-FU being used as positive control. The Ni- and V-complexes were the ones exhibiting the lowest IC_{50} values (<10 μM) in both human (A375 or HCT-116) cells (at 48 h of incubation), with the Fe(III) complex presenting minimal effects [23]. The encapsulation of the Ni- and V-complexes in nanoliposomes was used as a strategy to passively target them towards tumor cells [24]. The liposomal nanoformulation of the Ni-complex retained its antiproliferative properties against the melanoma cell lines, arrested the cell cycle at the G2/M phase, and showed no hemolytic activity, indicating suitability for intravenous administration. Preliminary studies in a subcutaneous murine melanoma model showed significant impairment of tumor progression at doses considerably lower than those required for 5-FU. Biodistribution studies further demonstrated preferential accumulation of the liposomal formulation at the tumor site, supporting the advantage of using nanoliposomes as drug delivery systems.

Nitrogen-containing heterocycles are a cornerstone of drug design: their ring nitrogen(s) provide hydrogen-bonding donor/acceptor sites and tunable basicity that directly shape target binding, metabolic stability, and membrane permeability. This structural leverage is reflected in their prevalence among approved therapeutics [33–35]. In the current paper, we report the synthesis of five Schiff base Ni(II)-complexes derived from 2-CHO-8HQ with amines containing the following N-heterocycles: morpholine, piperidine, imidazole and methylimidazole. The complexes were characterized in the solid state and in solution and their stability in aqueous media was evaluated by UV-Vis absorption spectroscopy. Since albumin is the most abundant protein in the plasma and a carrier of many exogenous molecules, spectroscopic studies were carried out to evaluate its interaction with the Ni complexes. The in vitro cytotoxicity of the complexes was evaluated on the human colon adenocarcinoma Colo205 cell line, as well as in a doxorubicin-resistant counterpart, the Colo320 cell line.

2. Results and Discussion

2.1. Characterization of the Ni(II) Compounds

Four new Ni(II) complexes were synthesized and characterized from 8-hydroxyquinoline Schiff base ligands previously reported (**1**, **2**, **4** and **5**) [21,25], while complex **3** has also been previously published [23]. In complexes **1**–**3** the R group contains morpholine or piperidine derivatives, while in complexes **4** and **5** these are derived from imidazole (Figure 1). The characterization in the solid-state and in solution confirm that the complexes contain two tridentate Schiff bases, were obtained in high purity and contain water molecules in the solid lattice. Their full characterization (elemental analysis, mass spectrometry, FTIR and UV–Vis spectroscopies) is included in Section 3, and Table 1 includes selected data.

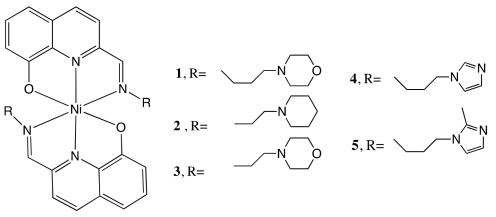

Figure 1. General structure of the reported Ni(II) complexes **1**–**5**.

Table 1. Selected data on the Ni(II)-complexes characterization (see Figures S1–S10).

Complex	$[M + H]^+$	ν(C=N)/cm^{-1}	λ_{em}/nm	LogD$_{7.4}$
1	655.02	1617	-	+0.097 ± 0.008
2	623.08	1628	-	+1.33 ± 0.04
3	627.07	1627	460	+0.26 ± 0.05
4	617.08	1633	450	Not stable
5	645.07	1627	450	+0.18 ± 0.02

The FTIR characterization (see Figures S1–S5) shows the presence of a strong stretching vibration band assigned to the C=N bond at ca. 1617–1633 cm^{-1} and broad bands centered at ca. 3000 cm^{-1} due to the presence of the water molecules. The sharp band at 1111–1115 cm^{-1} is attributed to the C-O$_{phenolate}$ stretching [36].

The UV–Vis spectra measured in dimethylsulfoxide (DMSO) show a charge transfer band at ~545 nm, n-π^* transitions of the azomethine groups at ca. 360 nm and strong intraligand π-π^* transition bands below 300 nm due to the 8HQ (and imidazole in **4** and **5**) aromatic rings. Figure S11 shows the spectra measured for all complexes in DMSO. Comparison with the spectrum measured in dichloromethane (DCM) for **1** confirms the charge transfer character of the lowest energy band, since it shows solvatochromism (see Figure S12) with a red-shift in the lower polarity solvent (DCM).

The luminescent properties of the compounds were studied in DMSO solutions. Several excitation wavelengths were used near the absorbance maxima of each compound. Complexes **1** and **2** showed no detectable emission under the conditions studied. Complex **3** showed emission when excited at wavelengths near the maximum of the $\pi \rightarrow \pi^*$ band. Both imidazole-derived complexes (**4** and **5**) exhibited fluorescence upon excitation at the $\pi \rightarrow \pi^*$ and n$\rightarrow\pi^*$ bands [37]; their emission spectra, recorded at approximately 10 µM, are included in Figure S13 and the emission maxima are included in Table 1.

2.2. Single-Crystal X-Ray Diffraction Characterization

While the single-crystal X-ray diffraction (SC-XRD) structure of complex **3** has been published [23], the structure of **1** will now be presented. Figure 2 displays the molecular structure, while the experimental part included in Section 3 and Table S1 provide the main crystallographic data, along with selected bond distances and angles. Complex **1** crystallizes in the orthorhombic system, space group Pbcn, forming a racemic crystal, containing both enantiomers. The structure features a distorted octahedrally coordinated Ni(II) center bound to two monodeprotonated NNO-tridentate ligands, adopting a meridional coordination mode, with the two oxygen atoms arranged cis to each other [O2-Ni-O2#1 = 97.19(9)°], as previously observed for **3** [23] and other related compounds [38]. The aromatic nitrogen atoms (N$_{quinoline}$) are positioned trans to one another [N11-Ni-N11#1 = 178.56(11)°], whereas the imine nitrogen atoms (N$_{imine}$) are located cis to each other [N14-Ni-N14#1 = 97.99(10)°].

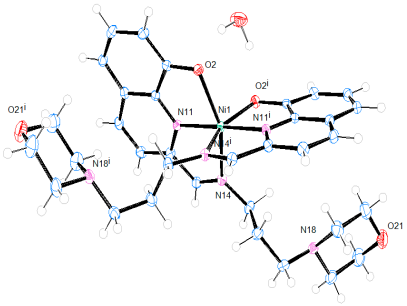

Figure 2. X-ray structure (ORTEP plot ellipsoids at 50% probability level) and labelling scheme for **1** determined by SC-XRD.

As observed in previous studies, the compound exhibits shorter Ni-$N_{quinoline}$ bond distances than Ni-N_{imine} bonds, consistent with the distinct electronic properties of the nitrogen atoms [21] and with the *trans* efect imposed by the $O_{phenolate}$ goups on the N_{imine} bonds. The Ni–N bond lengths are: Ni-N14, 2.1537(19) Å; Ni-N11 = 1.9777(18) Å. Moreover, the $N_{quinoline}$ is locked into a rigid, fused bicyclic aromatic system and that rigidity constrains the N-Ni-O bite angle. These bond lengths, along with the Ni-O distances, are consistent with reported values for related Zn(II) complexes [21]. These results are also consistent with values reported for V(IV) and Cu(II) complexes bearing the same ligands, despite presenting different coordination environments [23]. It is noteworthy that the Ni–N bond lengths are generally shorter than the Zn–N distances observed in complexes with analogous ligands and geometry [21]. This trend is consistent with the larger ionic radius of Zn^{2+} compared to Ni^{2+} (74 pm vs. 69 pm). Conversely, the Ni–O distances are longer than those of Zn–O (Table S2). These discrepancies may be attributed to the shorter, stronger Ni–N bonds arising from ligand-field stabilization. The resulting increase in electronic charge density at the metal center leads to greater inter-electronic repulsion; consequently, the complementary Ni–O bond elongates to mitigate this steric/electronic strain while maintaining the overall octahedral geometry. Interestingly, crystal structures were obtained for metal complexes of this ligand (4-(2-aminopropyl)morpholine) with V(IV)O, Ni(II), Cu(II) and Zn(II) and different geometries were obtained: square pyramidal with V(IV)O [23], square planar with Cu(II) [21] and octahedral with both Ni(II) and Zn(II) [21].

Intramolecular hydrogen bond interactions are observed between the neighboring ligands (H15A-O2, 3.177 Å) and between one water molecule and the two ligands (H1W-O2, 1.981Å) (Figure S14). The three-dimensional molecular arrangements of the compound along the a, b and c axis display intermolecular interactions involving the neighboring ligands and stabilizing the crystal lattice (Figure S15).

2.3. Lipophilicity of the Compounds

The lipophilicity of the compounds was studied by measuring their partitioning between two phases, *n*-octanol and HEPES buffer (pH 7.4), using the known shake-flask method [39]. LogD, or *n*-octanol/water distribution coefficient, measures the relative distribution of a compound between two immiscible phases: *n*-octanol (a lipophilic organic solvent) and water (or a polar hydrophilic buffer). Positive logD values indicate lipophilic compounds, and negative logD values indicate that the compound is more hydrophilic, preferring water over *n*-octanol. For all compounds, the $logD_{7.4}$ value is positive, indicating that the complexes are lipophilic (see Table 1). The most lipophilic is complex **2**, containing the piperidine moiety. For complex **4,** the time-dependent spectra recorded in *n*-octanol (see Figure S16) indicate that the compound is not stable in this solvent and thus, no logD value is presented.

2.4. Solution Studies

Characterization of the complexes in organic media and aqueous solution is essential to understand their stability and behavior in biological media. Therefore, absorption spectra were measured for all Ni(II) complexes in DMSO (Figure S17), in *n*-octanol (Figure S16), and in DMSO:HEPES buffer (10 mM, pH 7.4) (5%:95%) (Figure S18) for 24 h at two concentrations (ca. 40–70 and 200–300 μM). In organic solvents (DMSO and *n*-octanol), as no changes were observed, the complexes were considered stable (except for **4** in *n*-octanol, Figure S16). However, in aqueous media, all complexes showed changes over time (see Table 2 and Figure 3 for complex **1**). The observed absorbance changes, namely the presence of well-defined isosbestic points, are consistent with a reversible equilibrium between two species (Figure 3a,b) [40], probably due to one ligand dissociation: $NiL_2 \rightleftharpoons NiL + L$. This is supported by the observed intensity decrease at 480 and 294 nm and the appearance of a band at 380 nm. Figure S19 compares the initial and final spectra with the ligand in the same media that corroborates the partial release of the ligand.

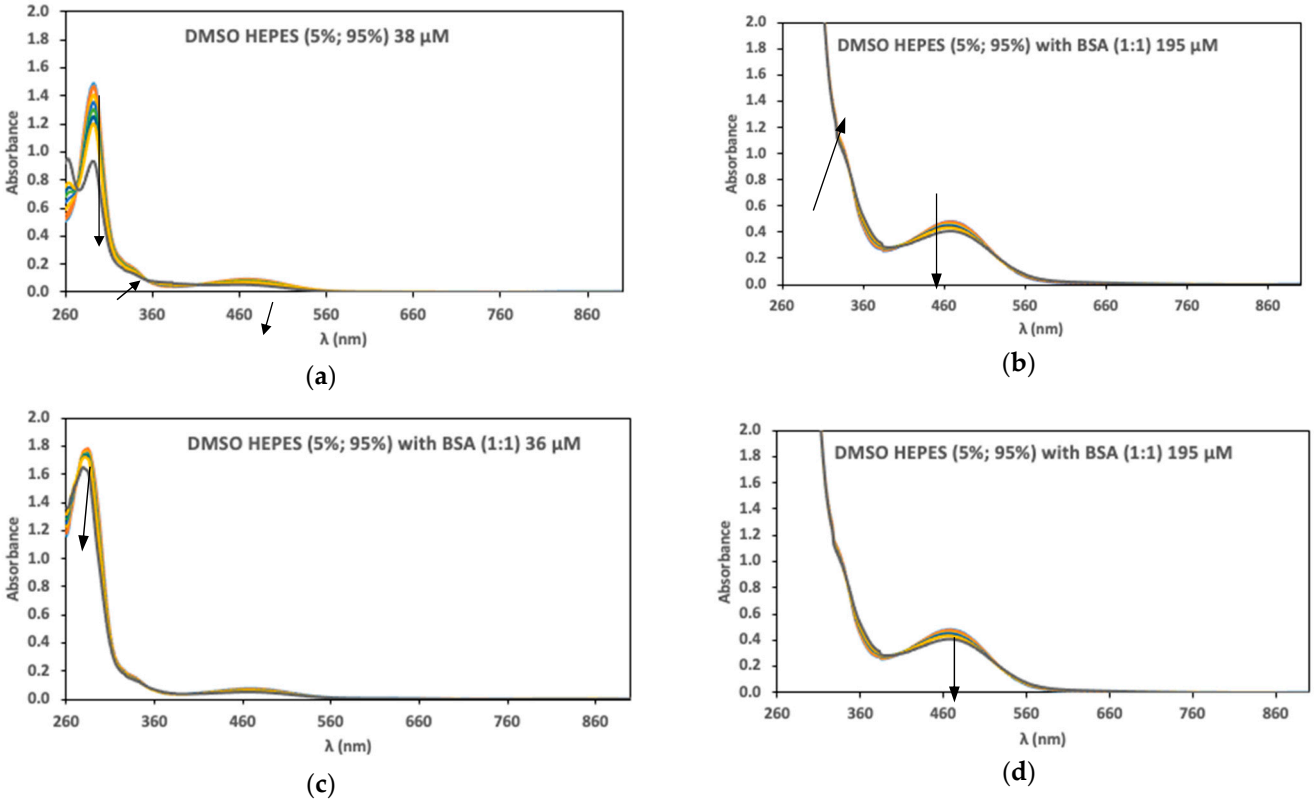

Figure 3. UV–Vis absorption spectra measured for complex **1** in aqueous media (DMSO:HEPES pH 7.4, 5%:95%) under different conditions, during 24 h. (**a**) without BSA, [1] = 38 μM; (**b**) without BSA, [1] = 195 μM; (**c**) BSA (1:1) molar ratio, [1] = 36 μM; (**d**) BSA (1:1) molar ratio, [1] = 195 μM. The arrows indicate time changes.

The addition of bovine serum albumin (BSA) in a 1:1 BSA:complex molar ratio decreases the spectral changes for most complexes, suggesting that the complexes bind to the protein (see Table 2 and Figure S18). The spectra measured for **1** in the absence and presence of BSA are shown in Figure 3. Decreased spectral intensity in the presence of BSA and strong albumin binding (K_{SV} ~10^6 M^{-1}, see below) indicates protein-assisted stabilization, supporting the use of 10% FBS in cytotoxicity assays [41].

Table 2. Spectral variations observed for the complexes in aqueous media, DMSO:HEPES buffer pH 7.4 (5%:95%). See the spectral variations in Figure S18.

Complex	Without BSA			With BSA (1:1)		
	λ/nm	c/μM	Variation	λ/nm	c/μM	Variation
1	293	40	Decrease, 37%	284	36	Decrease, 9%
	468	195	Decrease, 20%	467	195	Decrease, 15%
2	292	75	Decrease, 37%	277	15	Decrease, 4%
	466	280	Decrease, 10%	417	271	Decrease, 4.5%
4	293	60	Decrease, 20%	280	15	Decrease, 10%
	465	130	Decrease, 14%	461	127	Decrease, 6%
5	293	72	Decrease, 14%	279	36	Decrease, 2.4%
	467	170	Decrease, 10%	464	170	Decrease, 10%

2.5. Interaction with BSA

The time-dependent studies in the presence of BSA suggest that the Ni(II) complexes bind the protein and that they can be transported in plasma bound to albumin. Therefore, spectroscopic emission studies were performed to determine the binding strength of the complexes and estimate the binding sites number in albumin.

Fluorescence measurements are widely employed to investigate drug–protein interactions owing to their high sensitivity and selectivity. BSA contains two tryptophan residues in subdomain IB and within the hydrophobic pocket of subdomain IIA. Excitation of BSA at 295 nm selectively excites tryptophan, giving a strong emission band at ca. 340 nm [42,43]. Since Trp emission is sensitive to the polarity of its microenvironment, binding of a ligand in or near these sites quenches the emission and may also shift its maximum. The Stern–Volmer equation, $I_0/I = 1 + K_{SV}[Q]$, relates the emission intensity of the biomolecule in the absence (I_0) and presence (I) of a quencher [Q] [37].

The Stern–Volmer plots, included in Figure 4a and obtained at the maximum emission wavelength (see titration data in Figure S20), show that all complexes induce very strong quenching, with complex **3** imposing the strongest effect, followed by **2**. The least effective complexes are **1** and **5**, containing the morpholine with the longer chain and the methylimidazole. It can also be observed that the Stern–Volmer plots can be adjusted with second order polynomial equations. An upward curvature can arise from several processes: more than one quenching process taking place, static and dynamic [28], static quenching involving multiple binding sites, or more complex stoichiometries between metal, ligand and protein [44,45]. Self-association of BSA can also be induced by metal ions at low concentrations. Usually, this equilibrium constant is dependent on the concentration of metal ion but only important for BSA solutions above 10 μM, which is higher than that used in the fluorescence assays (2–3 μM) [46,47].

For comparison purposes, the linear regions of the plots (observed at lower quencher concentration) were fitted with the Stern–Volmer equation (Figure 4b) and the parameters are included in Table 3. All complexes show the same trend, with K_{SV} constants in the 10^5 range [$(1.3 \pm 0.2) \times 10^5$ M^{-1}], indicating strong quenching, consistent with BSA association; however, mixed static/dynamic quenching may be occurring, as well as the establishment of different equilibria with the formation of potentially different species: BSA-Ni(n), BSA-L, BSA-NiL_2, and NiL [44].

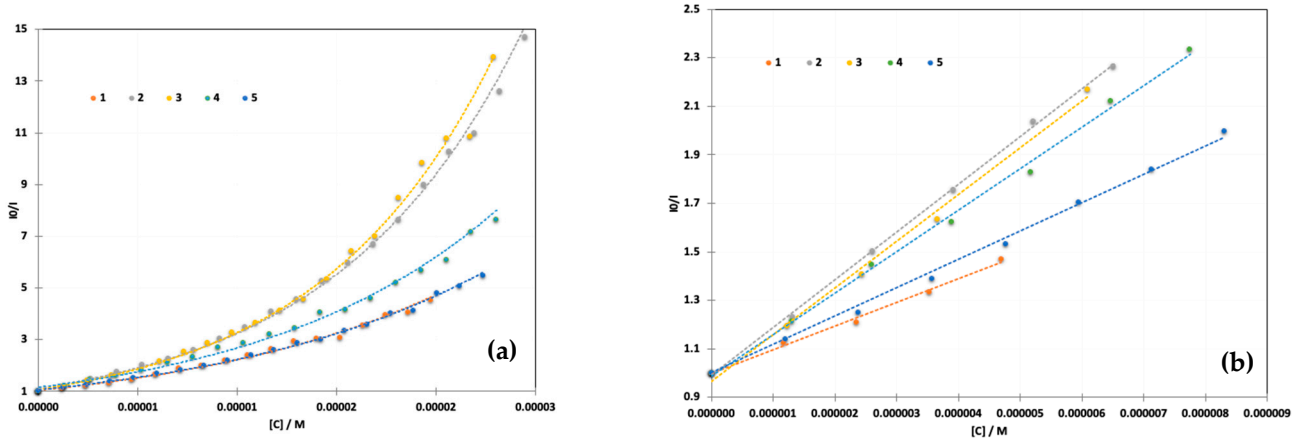

Figure 4. Stern–Volmer plot of the fluorescence quenching of BSA (λ_{exc} = 295 nm, λ_{em} = 340 nm) by complexes **1**–**5**, $c_{(BSA)}$~2–3 μM and %DMSO < 1.5% (*v*/*v*). (**a**) Full concentration range measured and (**b**) linear range.

Table 3. Parameters obtained for all Ni-complexes from the Stern–Volmer plot and the double logarithmic equation.

Compound	K_{SV}/M^{-1}	Intercept	R^2	K_a/M^{-1}	*n*	R^2
1	$(9.7 \pm 1.0) \times 10^4$	1.00 ± 0.04	0.994	3.6×10^6	1.3	0.994
2	$(2.0 \pm 0.3) \times 10^5$	0.99 ± 0.03	0.999	4.5×10^5	1.1	0.999
3	$(1.9 \pm 0.3) \times 10^5$	0.96 ± 0.09	0.994	2.3×10^6	1.2	0.997
4	$(1.7 \pm 0.1) \times 10^5$	0.99 ± 0.05	0.997	3.7×10^5	1.1	0.996
5	$(1.20 \pm 0.06) \times 10^5$	0.98 ± 0.03	0.998	1.0×10^5	1.0	0.996

Linearization of the quenching data at the maximum emission wavelength allows the estimation of the bimolecular association constant, K_a, and the number of binding sites on the protein (n), using the Benesi–Hildebrand Method [48] (double logarithmic equation):

$$log\left[\frac{I_0 - I}{I}\right] = n[Q] + logK_a \quad (1)$$

The binding constants obtained from the fitting are in the 10^5–10^6 M^{-1} range, suggesting strong binding, and are supported by the observed strong quenching. However, the fitting is sensitive to the range of data points included, and the derived values should therefore be interpreted with caution [44,49,50]. The binding model suggests that one binding site is occupied at the concentrations studied (*n* = 1.0–1.3).

2.6. In Vitro Cytotoxicity

The in vitro cytotoxicity of all (II) complexes (**1**–**5**) was assessed in the human colon adenocarcinoma Colo205 and the doxorubicin-resistant Colo320 cell lines. Table 4 collects the IC_{50} values determined at 72 h of incubation, with doxorubicin being used as the positive control. The Ni(II) complexes exhibited moderate cytotoxicity on both cancer cell lines (IC_{50} = 15.1–92.5 μM), being markedly less potent than doxorubicin. Complex **4** was found to be the most active complex on both cell lines, showing the lowest IC_{50} values (15.1 μM on Colo205 and 36.1 μM on Colo320), whereas **2** was the least active, especially against the resistant Colo320 cell line. The calculated resistance indices ranged between 1.3 and 3.1, which are comparable to or lower (thus, better) than that of doxorubicin (3.6), indicating that these Ni(II) complexes maintain significant activity against the resistant cell line.

Table 4. In vitro cytotoxicity of the Ni(II) complexes expressed in IC_{50} (μM) values, tested in various cancer cell lines (Colo205 and Colo320) at 72 h incubation time with doxorubicin as a positive control. Resistance index (RI = IC_{50}(Colo320)/IC_{50}(Colo205)) values are also shown.

IC_{50}/μM	Colo205	Colo320	RI
1	36.0 ± 4.0	61.5 ± 2.3	1.7
2	30.0 ± 2.7	92.5 ± 6.2	3.1
3	24.7 ± 3.1	37.3 ± 1.7	1.5
4	15.1 ± 1.2	36.1 ± 3.1	2.4
5	26.6 ± 1.2	34.7 ± 2.0	1.3
Doxorubicin	0.32 ± 0.04	1.14 ± 0.07	3.6

A limitation of the present cytotoxicity evaluation is that the free Schiff base ligands were not tested, meaning the reported IC_{50} values cannot unambiguously distinguish the contribution of Ni(II) coordination from the intrinsic bioactivity of the 8-hydroxyquinoline imine scaffold, which is often cytotoxic [51]. We previously screened the cytotoxicity of the ligands against malignant melanoma, A375 cells, and they showed IC_{50} values between 15.2 and 25.8 μM [21,25], with the corresponding Zn(II) and Cu(II) complexes being more active than the free ligands. The ligands present in complexes **4** and **5** were also screened against a series of cancer cell lines, showing IC_{50} values > 50 μM in most cells, except in MDA-MB-231, MCF-7 and BT549 (all breast cancer cells, 18 μM < IC_{50} < 38 μM), with the Zn(II) complexes being consistently more active than the free ligands [25]. Moreover, a previous report on complex **3** and its ligand demonstrated that the ligand had minimal impact on the viability of HCT-116 colon cancer cells (>80% viability at 40 μM), whereas **3** exhibited an IC_{50} of 5.9 ± 0.5 μM at 48 h [23]. This suggests that metal coordination plays a dominant role in the observed cytotoxicity, though the low selectivity of **3** for cancer cells over normal HaCaT cells remains a concern. Based on these observations, systematic evaluation of the free ligands was not pursued in the present study.

Tentative structure–activity trends can be drawn from pairwise comparison of the different substituents, with the limitation that the bioactive species has not been definitively identified; trends are therefore presented as correlations between pre-isolated complex identity and measured IC_{50} values, not as direct comparisons of isolated bis-chelate species in the assay matrix. Replacing the piperidine moiety (**2**) with morpholine (**3**) correlated with enhanced cytotoxicity, while lengthening the morpholine linker (**1**) correlated with decreased potency. The morpholine-to-imidazole (**4**) exchange yielded the most active compound, albeit with a slight increase in the resistance index. This is in agreement with imidazole being among the frequently appearing nitrogen heterocycles in small molecule drugs [52]. Methylation of the imidazole ring (**5**) reduced cytotoxicity against Colo205 but maintained activity against Colo320, resulting in the lowest resistance index (1.3), which may suggest reduced efflux recognition or altered cellular permeability, though confirmation would require dedicated transport studies.

2.7. Antibacterial Activity

The antibacterial activity of the Ni(II) complexes (**1**–**5**) was also studied on the Gram-positive *Staphylococcus aureus* and methicillin-resistant counterpart, as well as the Gram-negative *Escherichia coli* and *Klebsiella quasipneumoniae* strains. The tested compounds had no activity on these bacterial strains (minimum inhibitory concentration (MIC) > 100 μM), except for complex **5**, which displayed a moderate antibacterial effect against the *Staphylococcus aureus* strain (MIC = 50 μM).

3. Materials and Methods

3.1. Materials

8-hydroxy-2-quinolinecarboxaldehyde, 4-(2-aminoethyl)morpholine, 4-(2-aminopropyl) morpholine, 4-(2-aminoethyl)piperidine, 1-(3-aminopropyl)imidazole and 1-(3-aminopropyl)-2-methyl-1*H*-imidazole, nickel(II) chloride hexahydrate and 4-(2-hydroxyethyl)-1-piperazine ethanesulfonic acid (HEPES) were purchased from Sigma-Aldrich (St. Louis, MO, USA). Bovine serum albumin (BSA, Mw = 66,463 g/mol) was purchased from Sigma Aldrich, (St. Louis, MO, USA) and used without further purification (mass fraction purity $\geq$ 98%). HEPES buffer solutions (10 mM, pH = 7.4) (mass fraction purity $\geq$ 99.5%) were used as solvent to prepare the sample solutions at specific concentrations. All solutions were stored in a refrigerator at 4 °C in the dark. All the remaining reagents were of analytical grade and the deionized water was purified through a Millipore system (Burlington, MA, USA).

3.2. Apparatus

The electronic U–Vis absorption spectra were recorded with a PerkinElmer Lambda 35 spectrophotometer (Shelton, CT, USA). Infrared spectra (IR, 4000–400 cm^{-1}) were recorded on a Jasco FT/IR 4100 (Hachioji, Tokyo, Japan) or a Shimadzu IRAffinity-1S spectrophotometer (Kyoto, Japan) in KBr pellets. Elemental analysis for C, H, and N was carried out for the crude products on a FISONS EA 1108 CHNS-O apparatus (Milan, Italy) at the *Laboratório de Análises* of *Instituto Superior Técnico*. An LCQ Fleet ion trap mass spectrometer from Thermo Scientific (San Jose, CA, USA) was used to measure ESI-MS spectra of methanolic solutions of the compounds in both the positive and negative ion modes. Fluorescence measurements were carried out on an LS-55 spectrofluorometer (PerkinElmer, Shelton, CT, USA) equipped with a xenon pulse lamp. A quartz cell of 1.00 cm was used for the measurements. The slit widths for both excitation and emission wavelengths were set to 5 nm and the scan speed was 240 nm min^{-1}.

3.3. Synthesis and Characterization

For the synthesis of the nickel complexes, a one-pot reaction was used, starting with the ligand synthesis, similar to our previously reported compounds [21,25]. To a methanolic solution (20 mL) of the amine (2 mmol) and KOH (2 mmol), 8-hydroxy-2-quinolinecarboxaldehyde (2 mmol) was added. The resulting orange solution was stirred for 1 h at room temperature. Then, [$NiCl_2 \bullet 6H_2O$] (1 mmol) was added, and the resulting solution was stirred at room temperature for 2 h; subsequently, the solvent was evaporated. The solid precipitate was dissolved in dichloromethane, filtered, and recrystallized with *n*-hexane. Crystals suitable for SC-XRD were obtained for **1**.

Complex **1**—The amine used was 4-(2-aminopropyl)morpholine and an orange-red solid was obtained. Yield: 49%; elemental analysis calc. for $C_{34}H_{40}N_6NiO_4$ (655.43 g/mol) (+2 H_2O): C: 59.06, H: 6.41, N: 12.15. Found: C: 59.3, H: 6.0, N: 12.0. ESI-MS (+) m/z 655 $[M + H]^+$. UV-Vis: [DMSO, λ_{max}/nm ($\varepsilon/M^{-1}cm^{-1}$)]: 304 ($4.36 \times 10^4$); 370 (sh); 529 ($3.89 \times 10^3$); [$CH_2Cl_2$, λ_{max}/nm ($\varepsilon/M^{-1}cm^{-1}$)]: 305 ($4.5 \times 10^4$); 360 (sh, 6.3×10^3); 545 (3.69×10^3). FTIR [KBr, cm^{-1}]: 1617 ($\nu_{C=N}$), 1590 ($\nu_{C=C}$), 1481 ($\nu_{C=C}$), 1346 ($\nu_{C\text{-}N\ aromatic}$), 1116 ($\nu_{C\text{-}O}$), 1050), 860 ($\nu_{C\text{-}H\ aromatic}$), 837 ($\nu_{C\text{-}H\ aromatic}$), 743 ($\nu_{C\text{-}H\ aromatic}$).

Complex **2**—The amine used was 4-(2-aminoethyl)piperidine. Yield: 69%; elemental analysis calc. for $C_{34}H_{40}N_6NiO_2$ (623.43 g/mol) (+4.5 H_2O): C: 57.97, H: 7.01, N: 11.93. Found: C: 58.0, H: 5.5, N: 11.3. ESI-MS(+): m/z 623 $[M + H^+]$, 661 $[M + K]^+$. UV-Vis: [DMSO, λ_{max}/nm ($\varepsilon/M^{-1}cm^{-1}$)]: 265 ($3.70 \times 10^4$); 303 ($2.99 \times 10^4$); 352 (sh, 6.9×10^3); 430 (sh, 2.6×10^3); 542 (1.9×10^3). FTIR [KBr, cm^{-1}]: 1628 ($\nu_{C=N}$), 1588 ($\nu_{C=C}$), 1451 ($\nu_{C=C}$), 1348 ($\nu_{C\text{-}N\ aromatic}$), 1113 ($\nu_{C\text{-}O}$), 838 ($\nu_{C\text{-}H\ aromatic}$), 765 ($\nu_{C\text{-}H\ aromatic}$), 655 ($\nu_{C\text{-}H\ aromatic}$).

Complex **3**—The synthesis of this Ni-complex and its SC XRD structure were previously published by us [23].

Complex **4**—The amine used was 1-(3-aminopropyl)imidazole and an orange-red solid was obtained. Yield: 65%; elemental analysis calc. for $C_{32}H_{30}N_8NiO_2$ (617.33 g/mol) (+3 H_2O): C: 57.25, H: 5.40, N: 16.69. Found: C: 56.8, H: 5.0, N: 16.2. ESI-MS (+): m/z 617 $[M + H]^+$, 655 $[M + K]^+$. UV-Vis: [DMSO, λ_{max}/nm (ε/$M^{-1}cm^{-1}$)]: 269 (5.5×10^4); 305 (4.8×10^4); 360 (Sh, 7.8×10^3); 542 (5.5×10^3). FTIR [KBr, cm^{-1}]: IR (KBr disk): 1633 ($\nu_{C=N}$), 1591 ($\nu_{C=C}$), 1451 ($\nu_{C=C}$), 1344 ($\nu_{C\text{-}N\ aromatic}$), 1105 ($\nu_{C\text{-}N\ alyphatic}$), 837 ($\nu_{C\text{-}H\ aromatic}$), 740 ($\nu_{C\text{-}H\ aromatic}$).

Complex **5**—The amine used was 1-(3-aminopropyl)-2-methyl-1*H*-imidazole and an orange-red solid was obtained. Elemental analysis calc. for $C_{34}H_{34}N_8NiO_2$ (645.38 g/mol) (+4 H_2O): C: 56.92, H: 5.90, N: 15.62. Found: C: 57.0, H: 5.0, N: 15.5. ESI-MS (+): m/z 645 $[M + H]^+$. UV-Vis: [DMSO, λ_{max}/nm (ε/$M^{-1}cm^{-1}$)]: 266 (4.3×10^4); 304 (3.4×10^4); 367 (sh, 5.2×10^3); 544 (2.5×10^3). FTIR [KBr, cm^{-1}]: IR (KBr disk): 1627 ($\nu_{C=N}$), 1591 ($\nu_{C=C}$), 1450 ($\nu_{C=C}$), 1345 ($\nu_{C\text{-}N\ aromatic}$), 1112 ($\nu_{C\text{-}N\ alyphatic}$), 838 ($\nu_{C\text{-}H\ aromatic}$), 750 ($\nu_{C\text{-}H\ aromatic}$).

3.4. Single-Crystal X-Ray Diffraction

The experimental data were measured on a Bruker D8 QUEST ECO (Karlsruhe, Germany) three-circle diffractometer system equipped with a Ceramic X-ray tube (Mo Kα, λ = 0.71076 Å) and a doubly curved silicon crystal Bruker Triumph monochromator. The frames were integrated with the Bruker SAINT V8.40B (Bruker AXS LLC, Madison, WI, USA, 2019) software package using a narrow-frame algorithm. Data were corrected for absorption effects using the Multi-Scan method (SADABS, v2016/2). CCDC 2521285 contains the supplementary crystallographic data for this structure. These data can be obtained free of charge from the Cambridge Crystallographic Data Centre via http://www.ccdc.cam.ac.uk/data_request/cif (accessed on 4 September 2026).

A red plate crystal of $C_{34}H_{42}N_6O_5Ni$, (**1**) with approximate dimensions 0.080 mm × 0.200 mm × 0.280 mm was used for the data acquisition. The integration of the data using an orthorhombic unit cell yielded a total of 38,825 reflections to a maximum θ angle 28.32° (0.75 Å resolution), of which 4037 were independent (average redundancy 9.617, completeness = 99.8%, R_{int} = 4.23%, R_{sig} = 2.19%) and 3591 (88.95%) were greater than $2\sigma(F^2)$. The final cell constants of a = 11.4592(4) Å, b = 9.6594(4) Å, c = 29.3926(9) Å, volume = 3253.4(2) $Å^3$, are based upon the refinement of the XYZ-centroids of 9950 reflections above 20 σ(I) with 5.514° < 2θ < 56.61°. The ratio of minimum to maximum apparent transmission was 0.868. The calculated minimum and maximum transmission coefficients (based on crystal size) are 0.8390 and 0.9500.

The structure was solved and refined using the Bruker SHELXTL (v6.14) Software Package [53], using the space group Pbcn, with Z = 4. The final anisotropic full-matrix least-squares refinement on F^2 with 212 variables converged at R1 = 5.34% for the observed data and wR2 = 10.71% for all data. The goodness-of-fit was 1.234. The largest peak in the final difference electron density synthesis was 0.355 $e^-/Å^3$ and the largest hole was −0.488 $e^-/Å^3$ with an RMS deviation of 0.072 $e^-/Å^3$. On the basis of the final model, the calculated density was 1.375 g/cm^3 and F(000), 1424 e^-.

3.5. LogD$_{7.4}$ Determination

The shake-flask method was used to determine the complexes lipophilicity [54,55]. Three parallel experiments were performed for each sample. Flasks containing equal volumes of *n*-octanol and HEPES buffer (10 mM, pH = 7.4) were stirred together for 12 h to saturate both phases. The compounds were then dissolved in *n*-octanol saturated in HEPES and stirred again for 4 h. After that, UV–Vis measurements with several concentrations

of the compound (between 0.1 and 200 μM) in *n*-octanol saturated in HEPES (1:1) were prepared to obtain the calibration curves, which were used to determine the compound's concentration in both phases. The Log $D_{7.4}$ (distribution coefficient at pH 7.4) of each compound was determined using the following equation, where $c_{octanol}$ and c_{buffer} are the concentrations of the complex in *n*-octanol and HEPES buffer, respectively:

$$logD_{7.4} = log\frac{C_{octanol}}{C_{buffer}}$$

3.6. Interaction with BSA

The fluorescence emission spectra were recorded with λ_{ex} = 295 nm and the fluorescence emission data was collected between 310–500 nm. For the measurements, a quartz cell of 1.0 cm was used; the slit widths for both excitation and emission were set to 5 nm and the scan speed was 240 nm min^{-1}. The concentration of BSA was kept roughly constant at 1.5 μM and increasing volumes of the compounds were added to the solution. Each solution sample was allowed to equilibrate for 5 min, and then the fluorescence spectra were recorded.

To account for the inner filter effect and reabsorption interferences, UV absorption spectra were measured for each sample between 250 and 500 nm [56,57]. Appropriate blanks were measured (containing the same concentration of complex and no BSA) and subtracted to correct the fluorescence spectra.

3.7. In Vitro Cell Studies: Cell Lines and Culture Conditions and Cytotoxicity Assay

3.7.1. Cell Lines and Culture Conditions

Human colon adenocarcinoma cell lines Colo205 doxorubicin-sensitive (ATCC-CCL-222) and Colo320/MDR-LRP multidrug-resistant expressing ABCB1 (MDR1)-LRP (ATCC-CCL-220.1) were purchased from LGC Promochem (Teddington, UK). The cells were cultured in RPMI 1640 medium supplemented with 10% heat-inactivated fetal bovine serum, 2 mM L-glutamine, 1 mM sodium pyruvate and 10 mM HEPES and were incubated at 37 °C in a 5% CO_2, 95% air atmosphere. The cells were detached with Trypsin–Versene (EDTA, Sigma) solution for 5 min at 37 °C.

3.7.2. MTT Assay

The procedure was the same as previously reported [58].

Briefly, stock solutions of the compounds (10 mM in DMSO) were prepared and subsequently diluted in complete culture medium for evaluation of their antiproliferative activity against human colon adenocarcinoma cell lines. Doxorubicin (Merck, Darmstadt, Germany) served as a positive control. Cells were detached with Trypsin–Versene (EDTA), resuspended in the appropriate culture medium at 1×10^4 cells per 100 μL, and seeded into 96-well plates; medium control wells received medium only. Two-fold serial dilutions of each compound were prepared horizontally across the plate in 100 μL of medium, giving a final well volume of 200 μL.

Plates were incubated at 37 °C for 72 h, after which 20 μL of MTT (5 mg/mL stock) was added per well. Following a further 4 h at 37 °C, 100 μL of SDS solution (10% *w*/*v* in 0.01 M HCl) was added and the plates were left overnight at 37 °C. Optical density was recorded at 540/630 nm on a Multiscan EX ELISA reader (Thermo Labsystems, Cheshire, WA, USA).

Growth inhibition was expressed as IC_{50}, the concentration reducing cell growth by 50% relative to untreated controls. Values of $100 - ((OD_{sample} - OD_{medium\ control})/(OD_{cell\ control} - OD_{medium\ control})) \times 100$ were plotted against log[compound] and fitted to a sigmoidal dose–response model (variable and fixed slope compared) in GraphPad Prism Version 7.00

for Windows, Graph Pad Software, La Jolla, CA, USA, 2018. IC_{50} values represent at least three independent experiments.

3.8. Antibacterial Effect: Bacterial Culture and Determination of MIC Values

Antibacterial activity was evaluated against four reference strains: the Gram-positive *Staphylococcus aureus* ATCC 25923 (methicillin-susceptible) and *Staphylococcus aureus* ATCC 43300 (methicillin-resistant, MRS) and the Gram-negative *Escherichia coli* ATCC 25922 and *Klebsiella quasipneumoniae* ATCC 700603.

Minimum inhibitory concentrations (MICs) were determined by broth microdilution in 96-well plates, following Clinical and Laboratory Standards Institute guidelines [59]. Stock solutions of the compounds (5 mM in DMSO) were serially diluted in 100 µL of Mueller Hinton Broth per well. An overnight bacterial culture was diluted 10^{-4} in the same medium and 100 µL was added to each well, except the medium controls. Plates were incubated at 37 °C for 18 h, after which MIC values were read by visual inspection as the lowest concentration showing no visible growth.

4. Conclusions

Given the promising antiproliferative results obtained previously with a NiL_2 complex (**3**) in which L was a Schiff base derived from the condensation of 2-CHO-8HQ with 4-(2-aminoethyl)morpholine [23], four new Ni(II) complexes were prepared with Schiff bases containing other N-heterocycles—piperidine, imidazole, and methylimidazole—as well as a morpholine with a longer linker (propyl). These new complexes were characterized in the solid state and in solution, and a new SCXRD structure was obtained for the new morpholine complex. Both Ni(II) (**1** and **3**) complexes adopt essentially the same distorted-octahedral bis-tridentate NNO coordination, with meridional, cis phenolate oxygens, cis imine nitrogens and trans quinoline nitrogens, as well as closely comparable Ni–N and Ni–O bond lengths. The principal distinction is crystallographic rather than molecular: complex **3** crystallizes in $P2_1/n$ with two independent molecules on general positions [23], whereas complex **1** crystallizes in Pbcn with the molecule lying on a crystallographic twofold axis.

The spectroscopic solution characterization evidenced the stability of the Ni-complexes in organic solvents, with small changes being observed in aqueous media, which were considerably reduced in the presence of BSA. Since this protein is present in very high concentration in cell media, due to the cell's supplementation with FBS (fetal bovine serum), the complexes will probably be stabilized in the cell culture media. The fluorimetric quenching studies conducted with BSA corroborated the strong binding as K_{SV} constants in the 10^5 M^{-1} were obtained.

The Ni-complexes were screened against colon cancer cells, with a particular focus on doxorubicin-resistance, the Colo320 cell line. The Ni(II) complexes showed moderate cytotoxicity against both cell lines (IC_{50} = 15.1–92.5 µM), much less potent than doxorubicin but with resistance indices (1.3–3.1) comparable to or better than doxorubicin's (3.6), with complex **4** being the most active and complex **2** the least active. Further studies, including additional cells lines and assays to investigate the mode of cell death, should be carried out, but overall, these Ni complexes represent an interesting platform to develop new anticancer drugs.

Supplementary Materials: The following supporting information can be downloaded at https://www.mdpi.com/article/10.3390/inorganics14090239/s1, FTIR, ESI-MS and UV–Vis molecular spectra; data on the single Crystal X-Ray diffraction; the spectra related to the solution stability studies and the BSA binding titrations. Figure S1. FTIR spectrum of complex **1** measured in KBr disks; Figure S2. FTIR spectrum of complex **2** measured in KBr disks; Figure S3. FTIR spectrum

of complex **3** measured in KBr disks; Figure S4. FTIR spectrum of complex **4** measured in KBr disks; Figure S5. FTIR spectrum of complex **5** measured in KBr disks; Figure S6. A and B) ESI-MS spectrum of complex **1** in positive mode. C) Expected isotopic pattern for the protonated molecule; Figure S7. A and B) ESI-MS spectrum of complex **2** in positive mode. C) Expected isotopic pattern for the protonated molecule; Figure S9. A and B) ESI-MS spectrum of complex **4** in positive mode. C) Expected isotopic pattern for the protonated molecule; Figure S10. A and B) ESI-MS spectrum of complex **5** in positive mode. C) Expected isotopic pattern for the protonated molecule; Figure S11. UV-vis absorption spectra of complexes **1**–**5** measured in DMSO; Figure S12. UV-vis absorption spectra of complex **1** measured in DMSO and CH_2Cl_2; Figure S13. Fluorescence emission spectra measured for complexes **3**–**5** in DMSO with λ_{ex} = 340 nm; Figure S14. Intramolecular hydrogen bonds in complex **1**; Figure S15. Packing of complex **1** along the A) a axis, B) b axis and C) c axis; Figure S16. Stability of the complexes monitored by UV-Vis absorption for 24 h (concentrations indicated in the figures) in n-octanol; Figure S17. Stability of the complexes monitored by UV-Vis absorption for 24 h at two concentrations (indicated in the figures) in DMSO; Figure S18. Stability of complexes **2**, **4** and **5**, monitored by UV-Vis absorption for 24 h (concentrations indicated in the figures) in DMSO:HEPES (10 mM, pH 7.4) (5%:95%) in the absence and in the presence of BSA in 1:1 molar ratio; Figure S19. Stability of complex **1** monitored by UV-Vis absorption after dissolution and after 24 h and the free ligand in DMSO:HEPES (10 mM, pH 7.4) (5%:95%). Concentrations: A) [**1**] = 38 mM and [L] = 227 mM. B) [**1**] = 38 mM and [L] = 227 mM; Figure S20. Fluorescence emission spectra measured for the quenching of BSA (~2–3 μM) with complexes **1**–**5** (λ_{exc} = 295 nm, %DMSO < 1.5 (*v*/*v*). Arrows indicate spectral evolution with increasing complex concentrations (between 0 and 25 mM); Table S1. Selected bond lengths (Å) and angles (°) for complex **1**; Table S2. Selected bond lengths (Å) for $Zn(L3)_2$ and complex **1**.

Author Contributions: Conceptualization, I.C.; methodology, I.C. and É.A.E.; validation, I.C. and É.A.E.; formal analysis, S.M., L.C.-R., A.A. and M.D.; investigation, S.M., L.C.-R., A.A. and M.D.; data curation, S.M., L.C.-R., A.A., M.D., X.F. and I.R.; writing—original draft preparation, I.C.; writing—review and editing, I.C., A.M.M.A. and É.A.E.; supervision, I.C., É.A.E. and G.S.; funding acquisition, I.C. All authors have read and agreed to the published version of the manuscript.

Funding: This work was supported by Fundação para a Ciência e a Tecnologia (projects UID/00100/2025—DOI https://doi.org/10.54499/UID/00100/2025; UID/PRR/00100/2025—DOI https://doi.org/10.54499/UID/PRR/00100/2025 and LA/P/0056/2020—https://doi.org/10.54499/LA/P/0056/2020). The authors thank COST Action NECTAR (CA18202) supported by COST (European Cooperation in Science and Technology).

Institutional Review Board Statement: Not applicable.

Informed Consent Statement: Not applicable.

Data Availability Statement: The original contributions presented in this study are included in the article/Supplementary Material. Further inquiries can be directed to the corresponding author.

Conflicts of Interest: The authors declare no conflicts of interest.

References

1. Khoury, A.; Deo, K.M.; Aldrich-Wright, J.R. Recent advances in platinum-based chemotherapeutics that exhibit inhibitory and targeted mechanisms of action. *J. Inorg. Biochem.* **2020**, *207*, 111070. [CrossRef] [PubMed]
2. Johnstone, T.C.; Suntharalingam, K.; Lippard, S.J. The Next Generation of Platinum Drugs: Targeted Pt(II) Agents, Nanoparticle Delivery, and Pt(IV) Prodrugs. *Chem. Rev.* **2016**, *116*, 3436–3486. [CrossRef] [PubMed]
3. Alessio, E.; Guo, Z.J. Metal Anticancer Complexes—Activity, Mechanism of Action, Future Perspectives. *Eur. J. Inorg. Chem.* **2017**, *2017*, 1539–1540. [CrossRef]
4. Gianferrara, T.; Bratsos, I.; Alessio, E. A categorization of metal anticancer compounds based on their mode of action. *Dalton Trans.* **2009**, *38*, 7588–7598. [CrossRef] [PubMed]
5. Jia, P.; Ouyang, R.; Cao, P.; Tong, X.; Zhou, X.; Lei, T.; Zhao, Y.; Guo, N.; Chang, H.; Miao, Y.; et al. Review: Recent advances and future development of metal complexes as anticancer agents. *J. Coord. Chem.* **2017**, *70*, 2175–2201. [CrossRef]

6. Denkhaus, E.; Salnikow, K. Nickel essentiality, toxicity, and carcinogenicity. *Crit. Rev. Oncol./Hematol.* **2002**, *42*, 35–56. [CrossRef] [PubMed]
7. Buschini, A.; Pinelli, S.; Pellacani, C.; Giordani, F.; Ferrari, M.B.; Bisceglie, F.; Giannetto, M.; Pelosi, G.; Tarasconi, P. Synthesis, characterization and deepening in the comprehension of the biological action mechanisms of a new nickel complex with antiproliferative activity. *J. Inorg. Biochem.* **2009**, *103*, 666–677. [CrossRef] [PubMed]
8. Vijayan, T.; Batool, A.; Arumugam, S.; Park, Y.; Jang, H.Y.; Kim, J.; Sengottuvelan, N. Photoresponsive Nickel(II) Complex with Enhanced Anticancer Activity: Insights into Biomolecular Interaction and Theoretical Studies. *J. Med. Chem.* **2026**, *69*, 15374–15390. [CrossRef] [PubMed]
9. Zhao, C.; Chen, X.; Zang, D.; Lan, X.; Liao, S.; Yang, C.; Zhang, P.; Wu, J.; Li, X.; Liu, N.; et al. A novel nickel complex works as a proteasomal deubiquitinase inhibitor for cancer therapy. *Oncogene* **2016**, *35*, 5916–5927. [CrossRef] [PubMed]
10. Eskandari, A.; Flamme, M.; Xiao, Z.; Suntharalingam, K. The Bulk Osteosarcoma and Osteosarcoma Stem Cell Activity of a Necroptosis-Inducing Nickel(II)–Phenanthroline Complex. *ChemBioChem* **2020**, *21*, 2854–2860. [CrossRef] [PubMed]
11. Passeri, G.; Northcote-Smith, J.; Perera, R.; Gubic, N.; Suntharalingam, K. An Osteosarcoma Stem Cell Potent Nickel(II)-Polypyridyl Complex Containing Flufenamic Acid. *Molecules* **2022**, *27*, 3277. [CrossRef] [PubMed]
12. Abbass, L.M.; Belaidi, M.; Bufarwa, S.M.; Sadeek, S.A. Exploring the anti-colon cancer potential of febuxostat-based mixed metal complexes with 2,2-bipyridine: MTT assay, toxicity evaluation, prediction profiles, and computational studies. *Inorg. Chem. Commun.* **2025**, *178*, 114460. [CrossRef]
13. Ogawa, T.; Sinha, N.; Pfund, B.; Prescimone, A.; Wenger, O.S. Molecular Design Principles to Elongate the Metal-to-Ligand Charge Transfer Excited-State Lifetimes of Square-Planar Nickel(II) Complexes. *J. Am. Chem. Soc.* **2022**, *144*, 21948–21960. [CrossRef] [PubMed]
14. Zhang, R.; Zhou, Y.; Lin, Z.; Huang, X.-C.; Zhang, J.; Gao, S.; Zhang, J.-L. A light-activated nickel(ii)–antibiotic conjugate for synergistic antibacterial therapy. *Chem. Commun.* **2026**, *62*, 3798–3801. [CrossRef] [PubMed]
15. Zhou, X. Insights of metal 8-hydroxylquinolinol complexes as the potential anticancer drugs. *J. Inorg. Biochem.* **2023**, *238*, 112051. [CrossRef] [PubMed]
16. Gupta, R.; Luxami, V.; Paul, K. Insights of 8-hydroxyquinolines: A novel target in medicinal chemistry. *Bioorg. Chem.* **2021**, *108*, 104633. [CrossRef] [PubMed]
17. Oliveri, V.; Vecchio, G. 8-Hydroxyquinolines in medicinal chemistry: A structural perspective. *Eur. J. Med. Chem.* **2016**, *120*, 252–274. [CrossRef] [PubMed]
18. Ding, W.Q.; Lind, S.E. Metal Ionophores—An Emerging Class of Anticancer Drugs. *IUBMB Life* **2009**, *61*, 1013–1018. [CrossRef] [PubMed]
19. Ribeiro, N.; Bulut, I.; Pósa, V.; Sergi, B.; Sciortino, G.; Pessoa, J.C.; Maia, L.B.; Ugone, V.; Garribba, E.; Enyedy, É.A.; et al. Solution chemical properties and anticancer potential of 8-hydroxyquinoline hydrazones and their oxidovanadium(IV) complexes. *J. Inorg. Biochem.* **2022**, *235*, 111932. [CrossRef] [PubMed]
20. Ribeiro, N.; Albino, M.; Ferreira, A.; Escrevente, C.; Barral, D.C.; Pessoa, J.C.; Reis, C.P.; Gaspar, M.M.; Correia, I. Liposomal Formulations of a New Zinc(II) Complex Exhibiting High Therapeutic Potential in a Murine Colon Cancer Model. *Int. J. Mol. Sci.* **2022**, *23*, 6728. [CrossRef] [PubMed]
21. Côrte-Real, L.; Pósa, V.; Martins, M.; Colucas, R.; May, N.V.; Fontrodona, X.; Romero, I.; Mendes, F.; Pinto Reis, C.; Gaspar, M.M.; et al. Cu(II) and Zn(II) Complexes of New 8-Hydroxyquinoline Schiff Bases: Investigating Their Structure, Solution Speciation, and Anticancer Potential. *Inorg. Chem.* **2023**, *62*, 11466–11486. [CrossRef] [PubMed]
22. Coelho, M.P.; Farinha, P.F.; Côrte-Real, L.; Ribeiro, N.; Luiz, H.; Pinho, J.O.; Noiva, R.; Godinho-Santos, C.; Reis, C.P.; Correia, I.; et al. Liposomal nanoformulations of novel copper-based complexes exhibiting antimelanoma activity—In vitro and in vivo validation. *Int. J. Pharm.* **2025**, *677*, 125643. [CrossRef] [PubMed]
23. Lopes, J.; Côrte-Real, L.; Neto, Í.; Alborghetti, A.; Dejoux, M.; May, N.V.; Fontrodona, X.; Romero, I.; Antunes, A.M.M.; Reis, C.P.; et al. Novel 8-Hydroxyquinoline-Derived V(IV)O, Ni(II), and Fe(III) Complexes: Synthesis, Characterization, and In Vitro Cytotoxicity Against Tumor Cells. *Inorganics* **2025**, *13*, 150. [CrossRef]
24. Lopes, J.; Neto, Í.; Coelho, M.P.; Côrte-Real, L.; Fernandes, C.; Gano, L.; Correia, I.; Rodrigues, C.M.P.; Reis, C.P.; Gaspar, M.M. Liposomal formulations of novel metal-based complexes exhibiting high antitumor activity against melanoma. *Int. J. Pharm.* **2025**, *686*, 126317. [CrossRef] [PubMed]
25. Côrte-Real, L.; Sergi, B.; Yildirim, B.; Colucas, R.; Starosta, R.; Fontrodona, X.; Romero, I.; André, V.; Acilan, C.; Correia, I. Enhanced selectivity towards melanoma cells with zinc(ii)-Schiff bases containing imidazole derivatives. *Dalton Trans.* **2024**, *53*, 9416–9432. [CrossRef] [PubMed]
26. Kos, J.; Mitrović, A. Nitroxoline: Repurposing its antimicrobial to antitumor application. *Acta Biochim. Pol.* **2019**, *66*, 521–531. [CrossRef] [PubMed]
27. Jiang, H.C.; Taggart, J.E.; Zhang, X.X.; Benbrook, D.M.; Lind, S.E.; Ding, W.Q. Nitroxoline (8-hydroxy-5-nitroquinoline) is more a potent anti-cancer agent than clioquinol (5-chloro-7-iodo-8-quinoline). *Cancer Lett.* **2011**, *312*, 11–17. [CrossRef] [PubMed]

28. Sarıoğlu, A.O.; Sürmelihindi, B.; Sogukomerogullari, H.G.; Yumrutaş, P.; Morcali, M.H.; Kose, M. Preparation, characterization, single-crystal analysis, and cytotoxic assessment of complexes formed by Schiff base and 8-hydroxyquinoline co-ligand with Co(II), Ni(II), and Mn(II) metal ions. *Polyhedron* **2024**, *261*, 117129. [CrossRef]
29. Liu, Y.-C.; Song, X.-Y.; Chen, Z.-F.; Gu, Y.-Q.; Peng, Y.; Liang, H. Synthesis, crystal structure, DNA interaction and cytotoxicity of a dinuclear nickel(II) complex with 5,7-dichloro-8-hydroxylquinoline. *Inorg. Chim. Acta* **2012**, *382*, 52–58. [CrossRef]
30. Wang, Z.-F.; Wei, Q.-C.; Li, J.-X.; Zhou, Z.; Zhang, S.-H. A new class of nickel(ii) oxyquinoline–bipyridine complexes as potent anticancer agents induces apoptosis and autophagy in A549/DDP tumor cells through mitophagy pathways. *Dalton Trans.* **2022**, *51*, 7154–7163. [CrossRef] [PubMed]
31. Yang, Q.-Y.; Cao, Q.-Q.; Qin, Q.-P.; Deng, C.-X.; Liang, H.; Chen, Z.-F. Syntheses, Crystal Structures, and Antitumor Activities of Copper(II) and Nickel(II) Complexes with 2-((2-(Pyridin-2-yl)hydrazono)methyl)quinolin-8-ol. *Int. J. Mol. Sci.* **2018**, *19*, 1874. [CrossRef] [PubMed]
32. Ribeiro, N.; Farinha, P.F.; Pinho, J.O.; Luiz, H.; Mészáros, J.P.; Galvão, A.M.; Costa Pessoa, J.; Enyedy, É.A.; Reis, C.P.; Correia, I.; et al. Metal Coordination and Biological Screening of a Schiff Base Derived from 8-Hydroxyquinoline and Benzothiazole. *Pharmaceutics* **2022**, *14*, 2583. [CrossRef] [PubMed]
33. Ebenezer, O.; Jordaan, M.A.; Carena, G.; Bono, T.; Shapi, M.; Tuszynski, J.A. An Overview of the Biological Evaluation of Selected Nitrogen-Containing Heterocycle Medicinal Chemistry Compounds. *Int. J. Mol. Sci.* **2022**, *23*, 8117. [CrossRef] [PubMed]
34. Gomtsyan, A. Heterocycles in drugs and drug discovery. *Chem. Heterocycl. Compd.* **2012**, *48*, 7–10. [CrossRef]
35. Jadala, C.; Mishra, S.; Potuganti, G.R.; Cardoza, S.; Velma, G.R. Nitrogen-containing FDA-approved drugs in 2025: Synthesis, significance and therapeutic applications. *RSC Adv.* **2026**, *16*, 21967–22005. [CrossRef] [PubMed]
36. Nakamoto, K. *Infrared and Raman Spectra of Inorganic and Coordination Compounds: Part A: Theory and Applications in Inorganic Chemistry, Sixth Edition*, 5th ed.; Wiley: Hoboken, NJ, USA, 2008.
37. Lakowicz, W.R. *Principles of Fluorescence Spectroscopy*, 3rd ed.; Springer: Berlin/Heidelberg, Germany, 2006.
38. Hao, Z.Q.; Gao, T.Y.; Zhou, X.Y.; Ma, Z.H.; Han, Z.A.; Lu, G.L.; Lin, J. Nickel(II) complexes bearing 8-hydroxyquinoline-imine ligands: Synthesis and catalysis in hydrosilylation of aldehydes and ketones. *J. Mol. Struct.* **2023**, *1294*, 136539. [CrossRef]
39. Andrés, A.; Rosés, M.; Ràfols, C.; Bosch, E.; Espinosa, S.; Segarra, V.; Huerta, J.M. Setup and validation of shake-flask procedures for the determination of partition coefficients (logD) from low drug amounts. *Eur. J. Pharm. Sci.* **2015**, *76*, 181–191. [CrossRef] [PubMed]
40. Kaspar, F. Quality Data from Messy Spectra: How Isometric Points Increase Information Content in Highly Overlapping Spectra. *ChemBioChem* **2023**, *24*, e202200744. [CrossRef] [PubMed]
41. Levina, A.; Crans, D.C.; Lay, P.A. Speciation of metal drugs, supplements and toxins in media and bodily fluids controls in vitro activities. *Coord. Chem. Rev.* **2017**, *352*, 473–498. [CrossRef]
42. Huang, B.X.; Kim, H.Y.; Dass, C. Probing three-dimensional structure of bovine serum albumin by chemical cross-linking and mass spectrometry. *J. Am. Soc. Mass Spectrom.* **2004**, *15*, 1237–1247. [CrossRef] [PubMed]
43. Meti, M.D.; Nandibewoor, S.T.; Joshi, S.D.; More, U.A.; Chimatadar, S.A. Multi-spectroscopic investigation of the binding interaction of fosfomycin with bovine serum albumin. *J. Pharm. Anal.* **2015**, *5*, 249–255. [CrossRef] [PubMed]
44. Gamov, G.A. Processing of the spectrofluorimetric data using the graphical methods and the maximum likelihood approach. *Spectroch. Acta Part A Mol. Biomol. Spectrosc.* **2021**, *249*, 119334. [CrossRef] [PubMed]
45. Yarullin, D.N.; Zavalishin, M.N.; Sharnin, V.A.; Gamov, G.A. Equilibrium in a Bovine Serum Albumin–Pyridoxal-5-phosphate 4-Hydroxybenzoyl Hydrazone–La3+ Ion System. *Russ. J. Phys. Chem. A* **2022**, *96*, 1190–1194. [CrossRef]
46. Chatterjee, S.; Mukherjee, T.K. Effect of Self-Association of Bovine Serum Albumin on the Stability of Surfactant-Induced Aggregates of Allylamine-Capped Silicon Quantum Dots. *J. Phys. Chem. B* **2013**, *117*, 16110–16116. [CrossRef] [PubMed]
47. Levi, V.; González Flecha, F.L. Reversible fast-dimerization of bovine serum albumin detected by fluorescence resonance energy transfer. *Biochim. Biophys. Acta Proteins Proteom.* **2002**, *1599*, 141–148. [CrossRef] [PubMed]
48. Benesi, H.A.; Hildebrand, J.H. A Spectrophotometric Investigation of the Interaction of Iodine with Aromatic Hydrocarbons. *J. Am. Chem.l Soc.* **1949**, *71*, 2703. [CrossRef]
49. Macii, F.; Biver, T. Spectrofluorimetric analysis of the binding of a target molecule to serum albumin: Tricky aspects and tips. *J. Inorg. Biochem.* **2021**, *216*, 111305. [CrossRef] [PubMed]
50. Dömötör, O.; Binacchi, F.; Ribeiro, N.; Busto, N.; Gonzalez-García, J.; Garcia-España, E.; Correia, I.; Enyedy, É.A.; Hamacek, J.; Terenzi, A.; et al. How reliable is the evaluation of DNA binding constants? Insights and best practices based on an inter-laboratory fluorescence titration study. *Spectrochim. Acta Part A Mol. Biomol. Spectrosc.* **2025**, *327*, 125354. [CrossRef] [PubMed]
51. Côrte-Real, L.; Ribeiro, N.; Correia, I. Anticancer drugs based on metal complexes of 2-imine-8-hydroxyquinolines. *Front. Chem. Biol.* **2026**, *5*, 1734289. [CrossRef]
52. Vitaku, E.; Smith, D.T.; Njardarson, J.T. Analysis of the Structural Diversity, Substitution Patterns, and Frequency of Nitrogen Heterocycles among U.S. FDA Approved Pharmaceuticals. *J. Med. Chem.* **2014**, *57*, 10257–10274. [CrossRef] [PubMed]
53. Sheldrick, G.M. A short history of *SHELX*. *Acta Crystallogr. Sect. A* **2008**, *64*, 112–122. [CrossRef] [PubMed]

54. Poole, S.K.; Poole, C.F. Separation methods for estimating octanol–water partition coefficients. *J. Chromat. B* **2003**, *797*, 3–19. [CrossRef] [PubMed]
55. Enyedy, É.A.; Hollender, D.; Kiss, T. Lipophilicity of kinetically labile metal complexes through the example of antidiabetic Zn(II) and VO(IV) compounds. *J. Pharm. Biomed. Anal.* **2011**, *54*, 1073–1081. [CrossRef] [PubMed]
56. Coutinho, A.; Prieto, M. Ribonuclease T1 and alcohol dehydrogenase fluorescence quenching by acrylamide: A laboratory experiment for undergraduate students. *J. Chem. Educ.* **1993**, *70*, 425–428. [CrossRef]
57. Marques, J.T.; de Almeida, R.F.M. Application of Ratiometric Measurements and Microplate Fluorimetry to Protein Denaturation: An Experiment for Analytical and Biochemistry Students. *J. Chem. Edu.* **2013**, *90*, 1522–1527. [CrossRef]
58. Pivarcsik, T.; Kljun, J.; Rodriguez, S.C.; Alcaraz, D.C.; Rapuš, U.; Nové, M.; Várkonyi, E.F.; Nyári, J.; Bogdanov, A.; Spengler, G.; et al. Structural and Solution Speciation Studies on fac-Tricarbonylrhenium(I) Complexes of 2,2′-Bipyridine Analogues. *ACS Omega* **2024**, *9*, 44601–44615. [CrossRef] [PubMed]
59. Zimmer, B.L. Susceptibility Testing Process. In *Methods for Dilution Antimicrobial Susceptibility Tests for Bacteria That Grow Aerobically*; Clinical and Laboratory Standards Institute: Wayne, MI, USA, 2015; pp. 15–19.